Travelling Ionosphere Disturbance Signatures on Ground-Based Observations of the O(^1D) Nightglow Inferred from 1D Modeling

Fabio Vargas[1]

[1]University of Illinois at Urbana-Champaign

Key Points:

- In general conditions, traveling ionosphere disturbances (TID) of longer vertical wavelengths (λ_z >160 km) are more likely than shorter vertical wavelength TID to be observed from ground-based imagery of the O(^1D) nightglow.
- For high solar activity periods, the volume emission rate of the O(^1D) nightglow layer is thicker (larger FWHM) and peaks at higher altitudes due to a larger concentration of O_2 at higher altitudes in the thermosphere.
- Because the O(^1D) layer is thicker under high solar activity conditions, only TID of $\lambda_z > 360$ km are likely to be detected from ground-based observations. This explains the lower observation rate of TID in the O(^1D) nightglow all-sky imagery in high solar activity intervals.

Corresponding author: Fabio Vargas, fvargas@illinois.edu

Abstract

This paper reports our simulations of the volume emission rate (VER) of the O(^1D) redline nightglow perturbed by waves traveling across the thermosphere at around 250 km altitude. Waves perturb the electronic and neutral background densities and temperatures in the region and modify the O(^1D) layer intensity as it is captured by ground-based nightglow instruments. The changes in the integrated volume emission rate are calculated for various vertical wavelengths of the perturbations. We demonstrate that, as the solar activity intensifies, the vertical scales of most likely observable TID waves become larger. For high solar activity, we demonstrate that only waves presenting vertical wavelengths larger than 360 km are likely to be observed. The variation of the range of likely observable vertical wavelengths with the solar cycle offers a plausible explanation for the low occurrence rate of TID in measurements of the redline nightglow during high solar activity periods. We have compared our results with those of Negale et al. (2018) and Paulino et al. (2018) to verify that observed vertical wavelengths distribute around 140-210 km, in good correspondence with our predicted threshold wavelength $\lambda_z^t \sim$160 km for very low solar cycle period.

1 Introduction

Traveling ionosphere disturbances (TID) on the ionospheric plasma have been observed for several decades. The initial reports date from the 1950s, such as those of Munro (1950), Munro (1958), and Martyn (1950). A successful interpretation of this phenomenon describes the TID as a manifestation of atmospheric gravity waves (AGW) perturbing the plasma (Hines, 1960).

W. Hooke (1968) further extended the Hines (1960) theory to account for gravity wave perturbations on the ionospheric plasma to show that their primary effect is dominated by the ratio of the neutral-plasma collision frequency to the giro-frequency under the influence of the geomagnetic field at thermospheric altitudes. In the ionosphere, gravity waves impart the motion of the neutral gas parallel to the magnetic field to the ionization via collisional interactions. W. Hooke (1968) also showed that only certain gravity wave modes are capable of creating perturbations in the ionosphere, and waves imparting velocities of 20 m/s seemed capable of exciting TID of larger magnitudes,

given the right background conditions. W. H. Hooke (1970) showed the ionosphere response to gravity waves as dependent on the propagation azimuth of the wave perturbation, evidencing the anisotropy of the propagation direction of TID in the lower and upper ionosphere. He found that the anisotropy is a function of the wave parameters and the ionospheric conditions.

Later on, Francis (1974) simulated a spectrum of gravity waves generated above the mesosphere to identify the effects of direct waves and ground-reflected waves on the upper levels around 200-300 km. This simulation explained the sources of the traveling ionosphere disturbances. The large and medium scale TID could be better distinguished, with the large scales being less frequent than the medium scales because of their correlation with the high latitude phenomena in the auroral TID source region in times of magnetic storms (kp>5), and particle precipitation generation of AGWs via Joule heating with the Lorentz force ongoing on charged particles under the Earth's magnetic field at those locations. Francis (1974) also pointed out that TID could be periodic and non-periodic, with the non-periodic TID being observed as frequently as their periodic counterparts. However, the non-periodic TID would resemble medium scale only.

Medium scale TID (MSTID) are the focus of this paper because of the number of poorly understood aspects of their nature. The MSTID, as presented earlier, can be periodic or non-periodic; therefore, it is more difficult to identify their cause. Whereas many papers (Nishioka et al., 2009; Negale et al., 2018) have identified the main source of TID at high latitudes, there are accounts of MSTID being excited at equatorial latitudes (e.g., Shiokawa et al., 2009; Paulino et al., 2018) and mid-latitudes as well (Shiokawa et al., 2003; Martinis et al., 2010; Paulino et al., 2018).

Observations of MSTID have been made via ground-based imagery of the thermospheric redline nightglow corresponding to the O($^3P - ^1D$) transition line at 630 nm. Although MSTID are frequently observed, only few articles report the vertical scales of these observed thermospheric oscillations, primarily because of the lack of background information about neutral wind at the layer altitude. For instance, one of the few articles showing the spectral distribution the vertical scales of MSTID for data collected over a three-year period is that of Negale et al. (2018). Moreover, combined modeling

and observational studies of MSTID of several vertical scales are carried out only sparingly. For example, Porter et al. (1974) studied the behavior of the O(^1D) nightglow brightness under the influence of gravity waves from a purely theoretical perspective, comparing the changes in both the nightglow intensity and electron density, while Ogawa et al. (2002) presented a simplified model to account for TID oscillations in the neutral and electron densities to explain perturbations in the total electron content and in the redline nightglow observed over Shigaraki, Japan.

In this work, we model the O(^1D) emission perturbed by MSTID/AGW of various vertical wavelengths to show which wave scales would be promptly accessible from ground-based observations. The model concerns zenith observations of the redline using all-sky imagers, but can also be extended to any zenith-integrated atmosphere variable affected by TID/gravity waves, such as photometry of the nightglow or GPS-TEC observations. The results are obtained under regular atmospheric conditions and for different solar activity scenarios as well. The implications of our findings are then analyzed in light of observed MSTID scales and features obtained from the redline imagery technique.

2 Methodology

The approach used here is similar to that of Vargas et al. (2007) for the simulation of the mesospheric nightglow layers perturbed by gravity waves. Here, however, we have also implemented equations to account for perturbations on the ion and electron densities. Beyond that, we have also applied wave perturbations on the ion and electron temperatures in the same way as that for the neutrals temperature.

Fig. 1 presents the input parameters utilized in our simulations taken from the IRI2016 and NRLMSISE-00 models for Jan 01, 2016, corresponding to low solar activity conditions for (30.3°S, 70.7°W), the coordinates of the Andes Lidar Observatory (ALO), in Chile. Fig. 1a shows vertical profiles of the O, O_2 and N_2 (from NRLMSISE-00), and the O^+ ion and electron number densities (from IRI2016). Atomic nitrogen is constant throughout the range as used in Link and Cogger (1998). The temperature for ions T_i, electrons T_e, and neutrals T_n are also from the IRI2016 model and are in Fig. 1b. Input

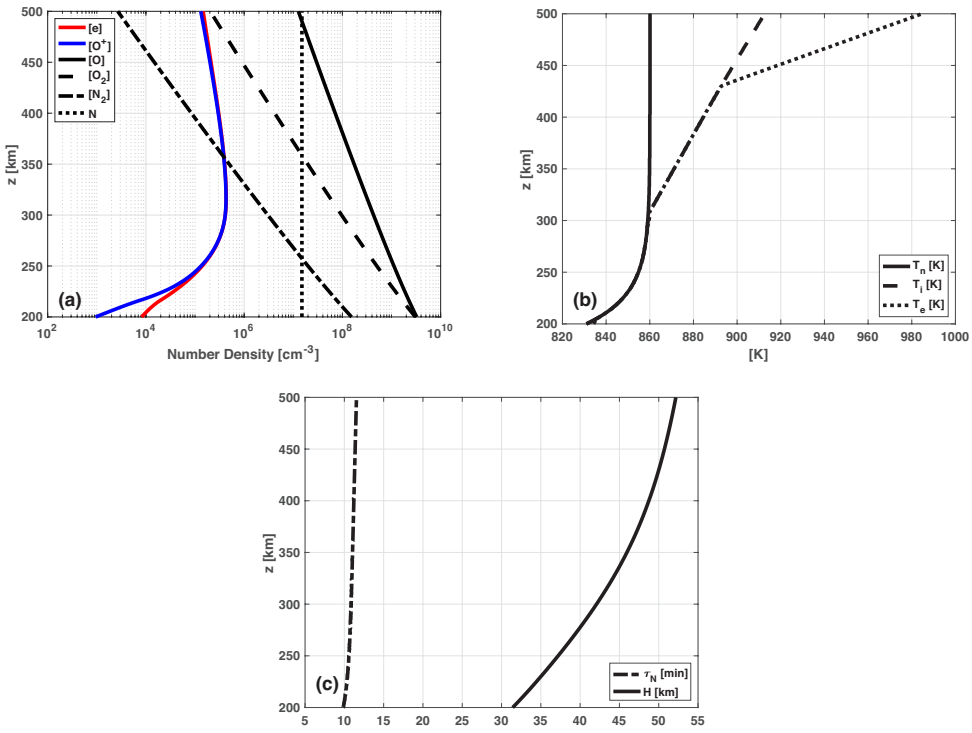

Figure 1. Background (a) densities, (b) temperatures, and (c) environmental parameters calculated for low solar activity conditions (Jan 01, 2016) for (30.3°S, 70.7°W), the coordinates of the Andes Lidar Observatory. Neutral densities are from the NRMSISE-00 model. Electron and ion densities, and neutral, electronic, and ionic temperatures are from the IRI2016 model. The input parameters for the NRMSISE-00 and IRI2016 models are in the supporting information file accompanying this publication.

parameters for the IRI2016 and NRLMSISE-00 models are given in the supporting information file accompanying this publication.

The environmental parameters in Fig. 1c are the Brunt-Väisälä period $\tau_N = 2\pi/N$, where N is the Brunt-Väisälä frequency, and the scale height for neutrals $H = Rs\overline{T}_n/M_{mw}g$, where $Rs = 8.31432\times10^3$ NmK^{-1}kmol^{-1} is the universal gas constant, M_{mw} the mean molecular weight, and g the gravity acceleration. The parameter N is given by $N = \frac{g}{\overline{T}_n}(d\overline{T}_n/dz + g/c_p)$, where $d\overline{T}_n/dz$ is the environmental lapse rate, g/c_p =9.8 K/km is the adiabatic lapse rate, and c_p is the specific heat at constant pressure.

Table 1. Chemical Reactions and Reaction Rates

	Reaction	Reaction Rate	Units	Reference
1	$O^+ + O_2 \rightarrow O_2^+ + O$	$k_1 = 3.23 \times 10^{-12} \exp\left(\frac{3.72}{(T_i/300)} - \frac{1.87}{(T_i/300)^2}\right)$	$cm^3 s^{-1}$	(Chen et al., 1978)
2	$O_2^+ + e \rightarrow O(^1D, ^1S) + O(^3P)$	$\alpha_1 = 1.95 \times 10^{-7}(T_e/300)^{-0.7}$	$cm^3 s^{-1}$	(Torr, Torr, Walker, Nier, et al., 1976)
3	$O(^1D) + N_2 \rightarrow O(^3P) + N_2$	$k_{N_2} = 2.00 \times 10^{-11} \exp(111.8/T_n)$	$cm^3 s^{-1}$	(Streit et al., 1976)
4	$O(^1D) + O_2 \rightarrow O(^3P) + O_2$	$k_{O_2} = 2.90 \times 10^{-11} \exp(67.5/T_n)$	$cm^3 s^{-1}$	(Streit et al., 1976)
5	$O(^1D) + O \rightarrow O(^3P) + O$	$k_O = 2.13 \times 10^{-12} + 2.60 \times 10^{-13} T_n^{0.5} - 2.44 \times 10^{-15} T_n$	$cm^3 s^{-1}$	(Yee et al., 1990)
6	$O(^1D) + e \rightarrow O(^3P) + e$	$k_e = 1.60 \times 10^{-12} T_e^{0.91}$	$cm^3 s^{-1}$	(Berrington & Burke, 1981)
7	$O_2^+ + N \rightarrow NO^+ + O$	$k_4 = 1.8 \times 10^{-1}$	$cm^3 s^{-1}$	(Ferguson, 1974)
8	$O^+ + N_2 \rightarrow NO^+ + N$	$k_{10} = 2.78 \times 10^{-13} \exp\left(\frac{2.07}{(T_i/300)} - \frac{0.61}{(T_i/300)^2}\right)$	$cm^3 s^{-1}$	(Chen et al., 1978)
9	$NO^+ + e \rightarrow N + O$	$\alpha_9 = 4.00 \times 10^{-7}(T_e/300)^{-0.9}$	$cm^3 s^{-1}$	(Torr, Torr, Walker, Brace, et al., 1976)
10	$O(^1D) \rightarrow O(^3P) + h\nu(6300)$	$A_{O(^1D)} = A_{6300} + A_{6364} = 6.81 \times 10^{-3}$	s^{-1}	(Link & Cogger, 1988)
11	$O(^1D)$ quantum yield for reaction 2	$f_{O(^1D)} = 1.10$	-	(Sobral et al., 1992)

[a]Footnote text here.

2.1 The O(^1D) Volume Emission Rate

To produce excited oxygen in the O(^1D) state in the ionosphere, the dissociative recombination of the molecular oxygen ion is the relevant process (reaction 2 in Table 1). The products of this reaction are oxygen atoms in the ground state O(^3P) and in the excited states O(^1D) and O(^1S), where the O(^1D) excited state is responsible for the thermosphere redline nightglow. The number of O(^1D) atoms produced from the dissociative recombination is determined by the quantum yield $f_{O(^1D)}$. The O(^1D) species can be deactivated by quenching of O, O_2, N_2, and electrons, as well as by the spontaneous radiation emission represented by $A_{O(^1D)}$. These reactions and their corresponding reaction rates are in Table 1.

To obtain the volume emission rate for the redline emission, we assume the photochemical equilibrium between production and losses, which leads to Eq. 1:

$$VER_{O(^1D)} = \frac{0.756\, A_{O(^1D)}\, f_{O(^1D)}\, k_1 [O_2][e]}{([e]/[O^+])(A_{O(^1D)} + k_O[O] + k_{O_2}[O_2] + k_{N_2}[N_2] + k_e[e])} \tag{1}$$

where

$$[e]/[O^+] = 1 + \left(\frac{k_1 O_2}{\alpha_1 [e] + k_4 [N]}\right)\left(1 + \frac{k_4 [N]}{\alpha_9 [e]}\right) + \frac{k_{10}[N_2]}{\alpha_9 [e]}$$

as given by Link and Cogger (1988).

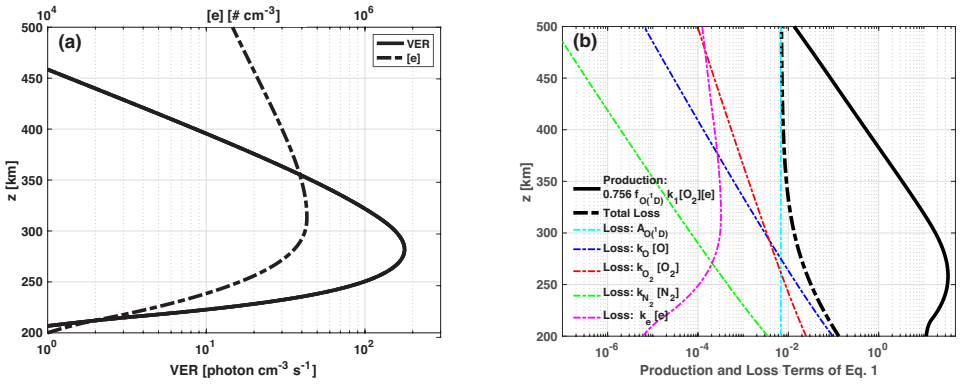

Figure 2. Low solar activity (a) unperturbed O(^1D) volume emission rate and electron density, and (b) production and loss terms of the O(^1D) volume emission rate from Eq. 1.

We evaluate Eq. 1 by plugging in the reaction rates in Table 1 and the numerical values of the quantities in Fig. 1a and Fig. 1b, and plot the unperturbed profile of the O(^1D) volume emission rate in Fig. 2a. The redline layer peaks at 282 km and presents 79 km full width at half maximum (FWHM) under the conditions simulated here. At the layer peak, the VER$\sim$180 photons/cm^3/s. For reference, we also plot in Fig. 2a the electron density profile (dash-dot line) to show its maximum about one scale height ($\sim$38 km) above the redline layer centroid. The unperturbed [e] density is much wider (FWHM$\sim$231 km) than the VER, and peaks at 323 km with a peak density of $\sim 4.6\times10^5$ electrons/cm^3.

Fig. 2b shows the contribution of individual production and loss terms in Eq. 1. The thick continuous line in Fig. 2b represents the production term corresponding to the numerator of Eq. 1, while the thick dash-dot line is the sum of all loss terms in the denominator. The thin dash-dot, colored lines are the individual losses. Note that the loss of the O(^1D) excited state due to the atomic oxygen dominates up to 275 km. Above that level the radiation term involving $A_{O(^1D)}$ dominates the loss of O(^1D). The term due to quenching by electrons is the least below 270 km, while the N_2 term is the smallest above that level.

2.2 Perturbing the O(^1D) Volume Emission Rate and Intensity

The O(^1D) volume emission rate response in the thermosphere to gravity waves is calculated by first obtaining the perturbations on the neutral and charge densities, vertical and horizontal winds, temperatures, and rate coefficients. To do so, we have set the characteristics of waves in terms of the vertical wavelength for a wave period taken from the 24 TID events observed by Paulino et al. (2018).

The layer brightness is the O(^1D) zenith intensity captured by nightglow imagers and photometers in ground-based experiments. We compute the O(^1D) intensity as the integral of the VER in altitude, where the VER is composed of the steady plus the perturbed states, that is, VER=$\overline{VER}$+VER', where $\overline{VER}$ corresponds to the curve in Fig. 2a. From the integral of the VER it follows that $I = \int VER\, dz = \int \overline{VER} + VER'\, dz = \overline{I} + I'$.

Other perturbed parameters are calculated as follows. According to the linear gravity wave theory (Hines, 1960), the wave frequency $\omega = 2\pi/\tau$, horizontal wavenumber $k = 2\pi/\lambda_h$ and the vertical wavenumber $m = 2\pi/\lambda_z$ are related by the dispersion relation (Eq. 2),

$$m^2 = \frac{(N^2 + \omega^2)}{(\omega^2 + f^2)}k^2 + \frac{\omega^2}{\gamma g H} - \frac{1}{4H^2} \tag{2}$$

where $\gamma = c_p/c_v$ is the specific heat ratio, and f is the Coriolis term. The parameters τ, λ_h, and λ_z are the intrinsic wave period, the horizontal wavelength, and the vertical wavelength of the perturbation, respectively. Notice that Eq. 2 holds for an isothermal atmosphere, what is nearly the case in the thermosphere. However, Eq. 2 does not take into account effects of viscous dissipation or heat diffusion dissipation on the gravity wave amplitudes. This is a limitation of the present simulation which must be addressed in an upcoming work.

Oscillations in the neutral density, temperature, and wind components are obtained from Eq. 3,

$$\left(u', w', \frac{\rho'}{\overline{\rho}}, \frac{T_n'}{\overline{T}_n}\right) = \Re\left\{(\hat{u}, \hat{w}, \hat{\rho}, \hat{T}_n) \exp\left[\frac{(1-\beta)(z-z_r)}{2H} + i\big[m(z-z_r) + \omega t\big]\right]\right\} \tag{3}$$

where u', w', $\rho'/\overline{\rho}$, and $T_n'/\overline{T}_n$ are the fluctuations in the wind component parallel to the wave orientation, the vertical wind, the neutral density, and the neutral temperature, respectively. The terms $\hat{u}, \hat{w}, \hat{\rho}, \hat{T}_n$ represent the complex amplitudes of each wave field. The total fields are given by $u = \overline{u} + u'$, $w = \overline{w} + w'$, $\rho = \overline{\rho} + \rho'$, and $T_n = \overline{T}_n + T_n'$.

The reference altitude z_r in Eq. 3 is set at 200 km where the wave amplitude $\hat{T}_n =$ 10%. The neutral temperature amplitude $\hat{T}_n$ is the reference parameter for the other quantities; that is, all other complex amplitudes are specified in terms of $\hat{T}_n$ via the polarization relations from the gravity wave linear theory.

The factor β in Eq. 3 accounts for the wave amplitude growth or decay. For $\beta <1$ the wave amplitude grows with increasing altitude, and for $\beta >1$ it decays. For $\beta =1$, the wave amplitude is constant, resembling the behavior of a saturated wave. We keep $\beta = 1$ in these simulations to straightforwardly quantify the effect of the wave perturbation in the O(^1D) layer throughout the simulation range. This makes sense because the layer response will be due solely to the layer's photochemistry and dynamics, once the relative wave amplitude $\hat{T}_n$ is constant everywhere.

The complex amplitudes $\hat{u}$ and $\hat{w}$ are given by the relations 4 and 5,

$$\hat{u} = \frac{\frac{gHk}{\omega}}{\frac{N^2}{N^2-\omega^2}\left(\frac{1}{2} + iHm - \frac{\kappa\omega^2}{N^2}\right)}\hat{T}_n \tag{4}$$

$$\hat{w} = \frac{\frac{ig\omega}{N^2-\omega^2}\left(\frac{1}{2} + iHm - \kappa\right)}{\frac{N^2}{N^2-\omega^2}\left(\frac{1}{2} + iHm - \frac{\kappa\omega^2}{N^2}\right)}\hat{T}_n\,, \tag{5}$$

while the complex amplitude for the neutral density $\hat{\rho}$ is given by Eq. 6.

$$\hat{\rho} = \frac{1 - \frac{2H\omega^2}{g(\gamma-1)} - 2iHm}{1 - \frac{2H\omega^2}{g} - 2iHm}\hat{T}_n \tag{6}$$

Perturbations in number densities of N_2, O_2, and N follow Eq. 6 as

$$\frac{[N_2]'}{\overline{[N_2]}} = \frac{[O_2]'}{\overline{[O_2]}} = \frac{[N]'}{\overline{[N]}} = \frac{\rho'}{\overline{\rho}}\,, \tag{7}$$

while atomic O perturbation follows Eq. 8,

$$\frac{[O]'}{\overline{[O]}} = DH\frac{\rho'}{\overline{\rho}} - \frac{1-DH}{\gamma-1}\frac{T_n'}{\overline{T}_n}\,, \tag{8}$$

where $D = \frac{d\ln[O]}{dz}$ is the scale height of the [O] density. The perturbed temperatures T_i and T_e follow that of the neutrals temperature, that is,

$$\frac{T_i'}{\overline{T_i}} = \frac{T_e'}{\overline{T_e}} = \frac{T_n'}{\overline{T}_n}\,. \tag{9}$$

The perturbation response of electrons due to the TID in the thermosphere is expressed as a function of the magnetic induction field $\vec{B}$ and the magnetic inclination angle as discussed in Hooke (1968). The total electron density is given by $[e] = \overline{[e]} + [e]'$. The fluctuation $[e]'$ is found from:

$$\frac{[e]'}{\overline{[e]}} = \left[\frac{(\vec{v}'\cdot\hat{B})(\vec{k}\cdot\hat{B})}{\omega}\right] + i(\hat{B}\cdot\hat{z})\left[\frac{1}{2H} + \frac{d}{dz}(\ln\overline{[e]})\right], \tag{10}$$

where the vector $\vec{v}' = u'\hat{\xi} + w'\hat{z}$ and $\vec{k} = k\hat{\xi} + m\hat{z}$. The unit vectors $\hat{z}$ and $\hat{\xi}$ are parallel to the vertical direction and to the wave orientation, respectively, and $\hat{B}$ is the unit vector parallel to $\vec{B}$. Observe from the term $(\vec{v}'\cdot\hat{B})$ that TID with stronger meridional component will have larger effect on the [e] density because $\vec{B}$ has a small zonal component. As confirmed in observations, equatorward traveling TID are promptly seen in ionospheric measurements (e.g., Francis, 1974; Shiokawa et al., 2006).

Temperature-dependent reaction rates are also affected by gravity wave oscillations via temperature oscillations. Perturbed states of the reaction rates are evaluated by plugging the perturbed temperatures into the corresponding reaction rate expressions (Table 1).

To carry out the simulations, we have chosen the vertical wavelength and the wave period as input parameters. A constant period of τ =45 min is set corresponding to one of 24 wave periods reported by Paulino et al. (2018) for TID perturbing the thermospheric redline. The vertical wavenumber $m = 2\pi/\lambda_z$ is specified iteratively, with λ_z varying from 50 km to 500 km by increments of 5 km. Then, we calculate $k = 2\pi/\lambda_h$

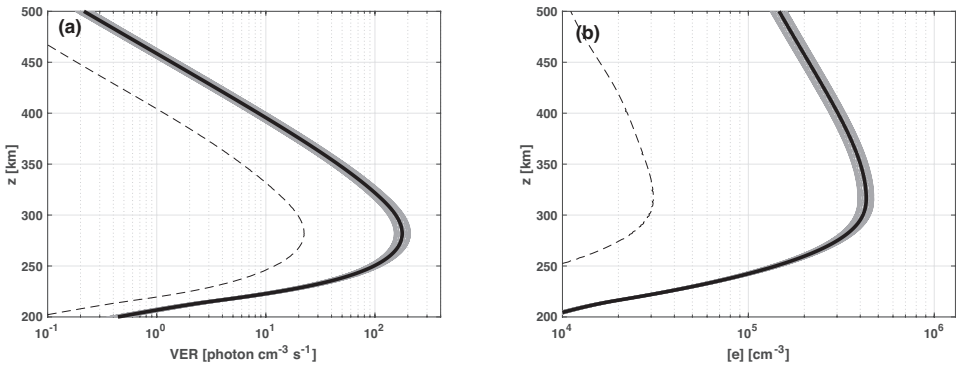

Figure 3. The perturbed (a) O(^1D) volume emission rate and (b) electron density calculated for 24 different phases of a perturbing gravity wave in a full wave cycle. The perturbing wave progresses vertically upwards in the thermosphere. The thick continuous lines are the unperturbed profiles of the VER and [e] as in Figure 2. The gray thin lines are the perturbed VER$'$ and [e]$'$ profiles. The dashed lines represent the standard deviation of the VER$'$ and [e]$'$ profiles, respectively. The perturbing wave has the following properties: λ_h= 852 km, λ_z= 230 km, τ= 45 min, $\hat{T}_n$= 10%, β= 1.

from the dispersion relation (Eq. 2) and the other perturbed quantities from Eqs. 4 to 9 within each iteration by setting $\hat{T}_n$ =10% of the background neutral temperature at the reference altitude. Notice that the horizontal wavenumber varies slightly with height due to variable environmental parameters τ_N and H (Fig. 1c).

Eq. 10 is evaluated by setting $\vec{B} = -69\,\hat{x} + 19956\,\hat{y} - 11937\,\hat{z}$ [nT], corresponding to components of the geomagnetic field at (30.3°S, 70.7°W) geographic coordinates and with -30.9° inclination angle with the horizontal plane at this location for the Andes Lidar Observatory, Chile. The unit vectors $\hat{x}$, $\hat{y}$, and $\hat{z}$ point toward the zonal, meridional, and vertical directions, respectively.

The relative perturbations are obtained for 1 km altitude resolution and $\frac{\tau}{24}$ time increments (this is equivalent to increments of 0.26 radians of the wave phase) within a wave cycle. All the perturbed quantities are finally plugged in Eq. 1 within each iteration to find the perturbed volume emission rate and intensity.

3 Results

The effect of wave perturbations on the redline layer VER is plotted in Fig. 3a. The perturbed VER profiles (gray thin lines) oscillate around the steady VER layer (thick continuous line), but the largest effect occurs at the peak at 286 km. The standard deviation σ_{VER} of the perturbed VER profiles is the dashed line in Fig. 3a, and confirms the higher variance around the layer peak height. The σ_{VER} profile indicates where the wave perturbation is more vigorous within the layer, which in the case of the O(^1D) occurs right at the peak of the thermospheric VER profile.

The altitude where σ_{VER} peaks is distinct for the mesospheric nightglow layers. In the mesosphere, σ_{VER} profiles of the OH, $O_2(b)$, and O(^1S) perturbed layers peak $\sim$2.5 km below their respective steady layer centroids (Vargas et al., 2007). This has a subtle impact on the interpretation of observational results when comparing data of the temperature and intensity of the mesospheric nightglows.

Fig. 3b shows the unperturbed [e] profile with amplitude of $\sim$9.5% at the peak of the unperturbed [e] layer (thick continuous line). The standard deviation $\sigma_{[e]}$ of the [e]' profiles is also presented as the dashed line. Similarly to the VER, $\sigma_{[e]}$ also shows large TID activity at the peak of the electron density profile.

Fig. 4 shows the time vs. altitude cross-section of (a) the temperature perturbation, (b) the perturbed O(^1D) VER, and (c) the perturbed electron density for a full wave cycle. The perturbing TID wave has the following properties: λ_h= 852 km, λ_z= 230 km, τ= 45 min, $\hat{T}_n$= 10%, β= 1. The TID has a discernible effect on the layer as it progresses vertically through the thermosphere. Fig. 4b demonstrates the changes in the VER. Observe that the layer peak height varies by about by $\pm$5 km during the wave period, while its thickness is as great as 78 km and as small as 62 km during the interval. Similarly, Fig. 4c shows that the TID causes the centroid of the [e] profile to go up (down) as the layer gets thicker (narrower), respectively.

The phase relationship among the perturbations in intensity, temperature, and vertical velocity due to the wave is in Fig. 5. The perturbation of the neutral temperature is opposite in phase to that of the intensity; that is, lower layer intensity corresponds to higher temperatures in the region, and conversely. On the other hand, the neutral

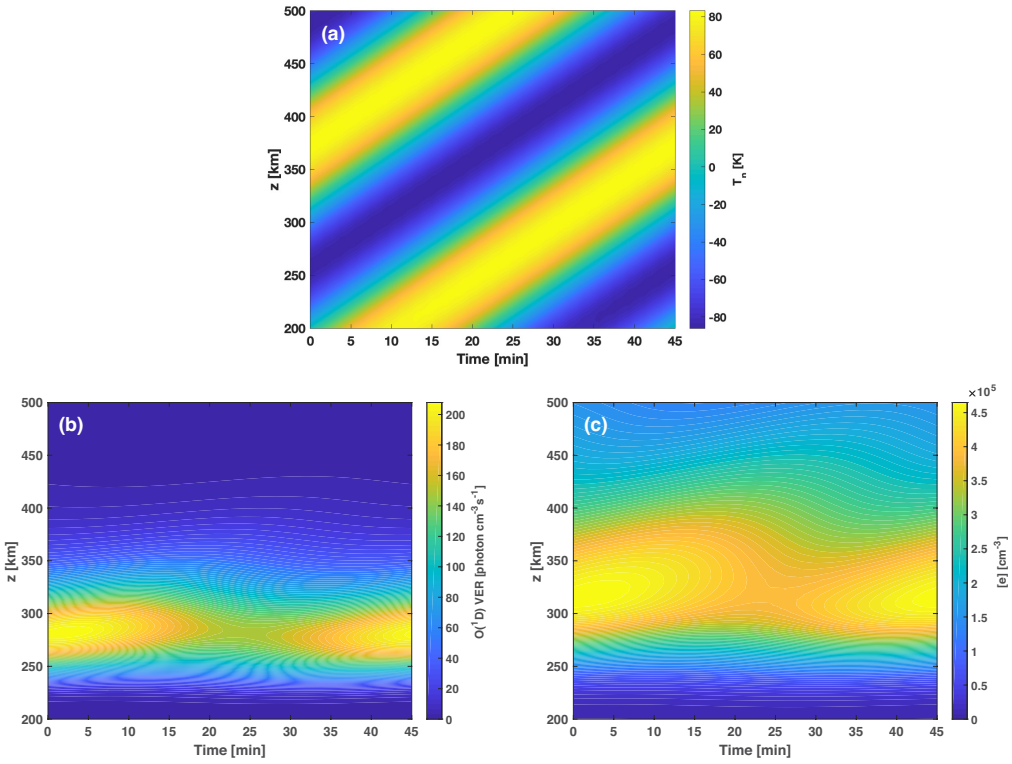

Figure 4. Time versus altitude cross-section of the (a) perturbed neutral temperature, (b) perturbed O(^1D) volume emission rate, and (c) perturbed electron density. The perturbing wave properties are the same as in Figure 3.

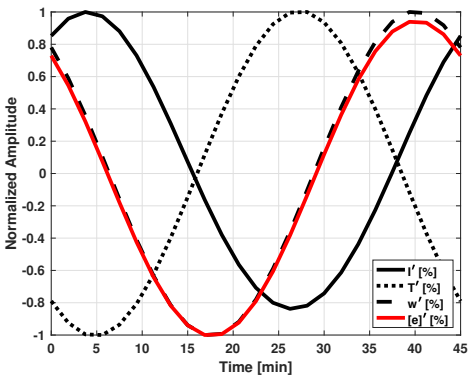

Figure 5. The phase of the vertical wind, neutral temperature, O(^1D) layer intensity, and electron density for a full wave period measured at the centroid altitude of the VER.

temperature and the vertical velocity perturbations are in phase quadrature as expected. The intensity and the vertical velocity perturbations are also in phase quadrature, with the vertical velocity leading in time. This translates to a brighter layer intensity as the wave moves particles upwards to a region of lower density around the VER peak where the quenching by N_2, O_2, and O is smaller. This causes less deactivation of the O(^1D) species and enhances the emission of 630 nm photons. Conversely, as the wave moves particles downward, the layer becomes dimmer.

The ratio of the relative perturbation in intensity $\frac{I'}{\bar{I}}$ to that in neutral temperature $\frac{T'}{\bar{T}_n}$ is also calculated (Fig. 6). This ratio, called the *cancellation factor* (CF=$\frac{I'/\bar{I}}{T_n'/\bar{T}_n}$), is used to determine how the layer responds to wave perturbations of various vertical scales. For a layer response in intensity larger than the input perturbation in temperature, the ratio CF is larger than the unit, indicating a gain or amplification of the wave perturbation in intensity. If the CF ratio is less than the unit, we interpret that as a suppression or attenuation of the wave perturbation.

The threshold vertical wavelength λ_z^t is defined as the wavelength for which cancellation factor ratio is equal to one. It is displayed in Fig. 6 by the vertical dotted line at $\lambda_z^t = 230$ km. Note that λ_z^t dissects the CF plot into two wavelength regimes, one for the $\lambda_z < \lambda_z^t$ range (attenuation regime) and the other for $\lambda_z > \lambda_z^t$ (amplification regime). The CF ratio decreases faster in the $\lambda_z < \lambda_z^t$ interval, indicating that the attenuation takes over rapidly in that regime. Waves in the $\lambda_z < \lambda_z^t$ regime will be more

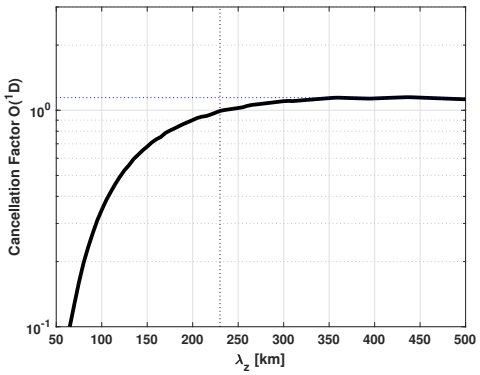

Figure 6. Calculated O(^1D) cancellation factor (the ratio of the relative intensity perturbation $\hat{I}$ to the relative neutral temperature perturbation $\hat{T_n}$) as a function of the vertical wavelength of a perturbing TID for low solar activity conditions. The horizontal dotted line marks the asymptotic value of the curve for longer vertical wavelengths. The vertical dotted line marks the threshold vertical wavelength where the relative layer intensity response $\hat{I}$ equals the relative input perturbation $\hat{T_n}$.

challenging to observe from ground-based measurements of the O(^1D) nightglow because the layer response in intensity decreases fast with decreasing wavelength.

In the attenuation regime ($\lambda_z < \lambda_z^t$), the cancellation factor indicates that the layer response is less than the input perturbation amplitude. For example, taking $\lambda_z = 100$ km, we see that CF(λ_z) $= 0.35$ from Fig. 6. The layer intensity response to a wave of such vertical scale is expected to be $I'/\overline{I} = T_n'/\overline{T}_n \times CF = 10\% \times 0.35 = 3.5\%$, corresponding to a much smaller amplitude in intensity and a strong attenuation of the original input perturbation due to the layer structure and thickness.

In the amplification regime ($\lambda_z > \lambda_z^t$), especially for the longer wavelength range, the asymptotic value of the CF ratio is 1.12. Thus, given an original input perturbation of $T_n'/\overline{T}_n$ =10 %, the maximum layer response in intensity is expected to be $I'/\overline{I} = T_n'/\overline{T}_n \times CF = 10\% \times 1.12 = 11.2\%$, indicating a small but welcome amplification of the wave amplitude in brightness for TID of larger vertical scales ($\lambda_z > \lambda_z^t = 230$ km). For this reason, the simulation suggests that TID in the amplification regime are more regularly detectable and identifiable in ground-based measurements because of the enhancement of the TID amplitude acting on the thermospheric redline nightglow.

Nonetheless, the asymptotic value of the O(^1D) layer is notably smaller than those calculated for the mesospheric nightglow layers (Vargas et al., 2007). For the mesospheric OH layer, the asymptotic CF value is 3.5, while it is 4.5 for the mesospheric O(^1S) greenline layer. This implies that, for an original perturbation of equal magnitude, we would notice a brighter wave perturbation from the mesospheric greenline layer than from the thermospheric redline layer. This expected behavior is due to the fact that a layer's response to an initial wave perturbation is linked to the distinct vertical structures and photochemistries of each nightglow layer.

4 Discussion

To understand how likely a TID is to be detected from ground-based observations of the O(^1D), we first demonstrate the variations in the redline layer structure, and then how the VER responds to waves of various vertical scales in different environmental conditions. These environmental conditions are set considering the solar cycle under (1) very low (F10.7= 66 solar flux units for 3-month average), (2) low (F10.7= 105 solar flux units for 3-month average), and (3) high activity (F10.7= 201 solar flux units for 3-month average) regimes. The input parameters for the IRI2016 and NRLMSISE-00 models to obtain the background variables for each solar cycle regime are specified in the supporting information file accompanying this publication and correspond to the location of the Andes Lidar Observatory (30.3°S, 70.7°W) because we want to utilize the results of this work in the investigation of TIDs observed over ALO.

The top panels in Fig. 7 show that the VER thickens and peaks at higher altitudes as the solar activity increases. For instance, for the very low conditions (Fig. 7a), the VER profile is 64 km wide and has centroid at 282 km. The VER for the low solar activity interval (Fig. 7b) peaks at 282 km and presents 79 km FWHM. On the other hand, the layer is 119 km thick and peaks at 343 km in the high solar cycle scenario (Fig. 7c).

We have performed sensitivity tests to determine which factor plays a major role in the changes of the O(^1D) layer structure as the solar cycle evolves. We have found that, even though temperature changes in the thermosphere are quite remarkable, they cause negligible effects in the VER because direct changes in temperature affect the re-

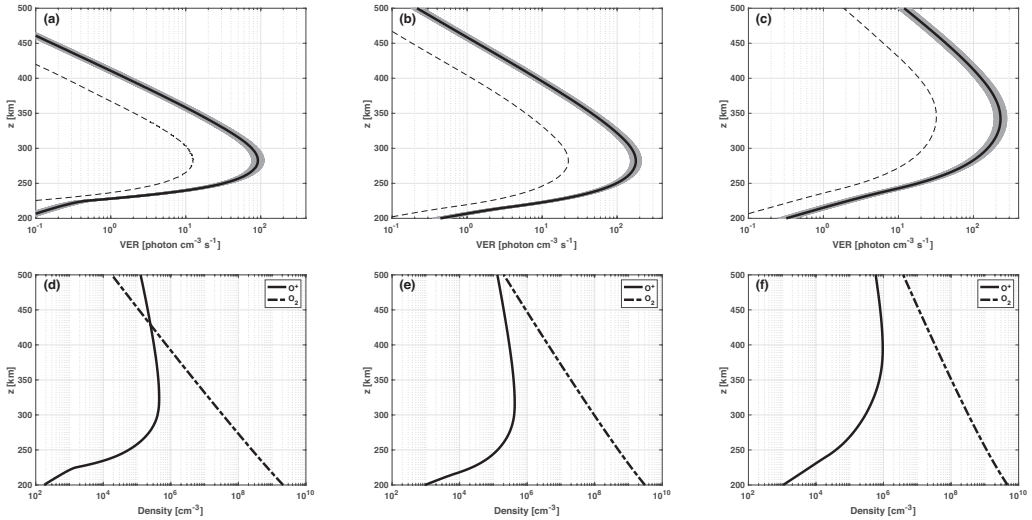

Figure 7. The top charts depict the O(^1D) VER for (a) very low, (b) low, and (c) high solar activity. The bottom charts depict the electron and molecular oxygen densities for (d) very low, (e) low, and (f) high solar activity.

action rates, which are small quantities of magnitude from 10^{-13} to 10^{-7}. Similarly, changes in the O, N_2, and N densities also have a minor effect on the layer's structure.

The charge density peak altitude also changes with the solar cycle. This can be verified from the thick lines in Figs. 7d, e, and f, which represent the ion density in the thermosphere for the simulated conditions. Above ∼240 km the ion density coincides with the electron density assuming the plasma neutrality principle, and both profiles peak at the same altitude. Although changes in the charge density are not small, we have verified that they are not the primary factor impacting the changes in the VER structure. We have tested this by taking the electron density from the high solar cycle period and plugging it into the very low and low solar activity scenario simulations. From that, we have seen only negligible changes in the VER structure. This is expected from the photochemistry standpoint once the quenching of the excited O(^1D) atoms by electrons represents the smallest loss term in Eq. 1 as depicted in Fig. 2b.

On the other hand, for example at 250 km, the O_2 density changes by about one order of magnitude from very low to high solar cycle scenarios (dashed-dot lines in Figs. 7d, e, and f, respectively). By taking the O_2 density from the high solar cycle period and

plugging it into the very low and low solar activity scenario simulations, we have verified major changes in the O(^1D) VER structure as well as in the layer thickness and in the layer peak altitude.

In Table 1, even though the dissociate recombination (reaction #2) is responsible for the production of the atomic oxygen in the ^1D excited state, the charge exchange (reaction #1) is the rate-determining reaction (Shiokawa et al., 2006). Thus, with a higher density of O_2 available in the thermosphere during the high solar cycle, we expect to see a brighter O(^1D) nightglow with a thicker VER profile peaking at higher altitudes. Because the [O^+] changes are much smaller than those in [O_2] as the solar cycle progresses, we attribute the O(^1D) VER changes simulated here to the [O_2]. The O_2 density increase with solar cycle is due to the expansion of the atmosphere due to the higher temperatures, which cause the densities of all constituents to increase in the upper thermospheric levels. Molecular diffusion also increases due to the markedly higher temperature, and so do the scale heights of the individual atmospheric constituents (Vickers et al., 2014; Swenson et al., 2018).

Thicker VER profiles, as discussed before, have direct impact on the observations of TID from the Earth's surface. To show how this occurs, we plot in Fig. 8 the CF ratios for three different solar activity scenarios, showing the tendency of the threshold vertical wavelength λ_z^t to increase accordingly. For instance, observe in the CF curve for the very low solar activity (dotted line) that λ_z^t =160 km , while for the high solar activity scenario λ_z^t =360 km (dash-dotted line in Fig. 8). The high solar activity λ_z^t is nearly double that of the very low solar activity scenario. Thus, we expect more difficulties in observing TID in the redline emission as the solar activity increases because the range of strong attenuation ($\lambda_z < \lambda_z^t$) shifts to ever larger vertical scales.

The cancellation effect described by the CF ratio is more effective for waves with vertical wavelengths smaller than or comparable to the layer thickness. For example, if the wave vertical scale is of the order of the layer thickness, the the wave will present positive (negative) phase above the layer peak and negative (positive) phase below the peak. Because the intensity is the vertical integral of the VER, the positive part above the peak cancels out the negative part below, resulting in a very attenuated wave amplitude from the ground. As the layer gets thicker as the solar activity increases, the

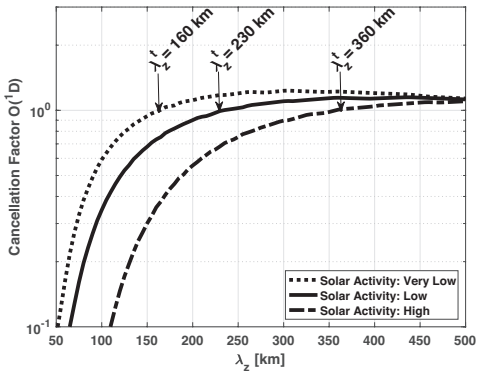

Figure 8. The O(^1D) cancellation factor for different solar activity scenarios. Note that the threshold vertical wavelength (the wavelength where CF=1) increases with solar activity.

attenuation starts affecting the larger wavelengths as well, and only longer vertical scale TID will be detectable.

The low occurrence rate of TID in the O(^1S) layer during high solar cycle has been confirmed by observational data (e.g., Garcia et al., 2000; Shiokawa et al., 2003; Candido et al., 2008; Pimenta et al., 2008; Park et al., 2010; Martinis et al., 2010). For instance, Bowman (1992) and Park et al. (2010) reported an inverse sunspot cycle occurrence rate of MSTID. Candido et al. (2008) showed that the maximal occurrence rate of MSTID happens during solar minimum. Nonetheless, Fedorenko et al. (2013) claim that TID occurrence does not depend on the sunspot number, while Klausner et al. (2009) show that TID have larger amplitudes during high solar activity. Thus, there are still opportunities for deeper investigation of the occurrence rate of TID around the globe to confirm these reports.

The Perkins instability (Perkins, 1973) has been invoked in many papers as the cause of the low occurrence of TID during high solar activity in mid latitude observatories (Taylor et al., 1998; Shiokawa et al., 2003; Nishioka et al., 2009; Takeo et al., 2017). The negative correlation with the solar activity is explained in terms the growth rate of the Perkins instability; that is, if the growth rate is large, which coincides with periods of low solar activity, the generation of MSTID is also large (Duly et al., 2013; Lakshmi Narayanan et al., 2014). However, Yokoyama and Hysell (2010) and Kubota et al. (2011) argue that the Perkins instability does not contribute to the generation of MSTID.

Other investigators show that neither the propagation direction (southwestward orientation) nor the scale size of TID is predicted correctly by the Perkins instability theory (Kotake et al., 2007; Shiokawa et al., 2009). Also, Paulino et al. (2016) show that TID wavefronts are not northeast-southwest oriented, in disagreement with Perkins instability predictions. Thus, while the Perkins instability role in the MSTID generation is still controversial, our model offers a simpler explanation for the low occurrence rate of TID in the high solar activity intervals in terms of the attenuation of the wave's amplitude. It is due to the redline layer vertical structure that benefits the observation of longer rather than shorter vertical wavelength TID.

Only a few studies provide the vertical scales of the observed TID. For instance, Negale et al. (2018) show that the measured fall seasonal day/night distribution of MSTID at high latitudes in the northern hemisphere presents a vertical wavenumber spectrum distributed around 273 km (mean) and 216 km (median). This is in good agreement with the threshold vertical wavelength shown in Fig. 8 for the low solar activity curve. Moreover, the vertical wavelength distribution measured by Negale et al. (2018) peaks at 230 km for the altitude range of 200-250 km, while the λ_z distribution peaks at $\sim$190 km within the altitude between 250-300 km. It is remarkable that only a few waves are present in the vertical wavelength range larger than 400 km. Thus, with few very long wavelength TID present in the spectrum in combination with the cancellation/attenuation effect for waves presenting $\lambda_z < \lambda_z^t$, we anticipate it should be harder to observe TID during high solar activity periods, and only dominant waves presenting larger amplitudes are likely detectable from ground-based measurements.

Paulino et al. (2018) also provided a climatology for TID observed in imagery of the redline nightglow from 2012-2014 (rising phase of the solar cycle 24) observed near the equatorial region at (7.4°S, 36.7°W) over the Brazilian sector. They did not calculate the vertical wavelength of the observed waves but provided a detailed table of wave features that permitted us to calculate and plot the histogram of the vertical wavelength distribution shown in Fig. 9. The wavelengths in the histogram are estimated using atmosphere background information from the NRLMSISE-00 and IRI2016 models for July 16, 2012 (F10.7=128 sfu, 3-month average) because most of the events were observed in 2012. To obtain the vertical wavelength, we have used Eq. 2. For instance, taking event 22 from

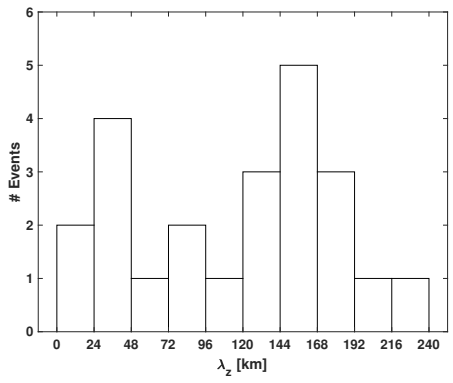

Figure 9. Distribution of observed vertical scales of TID/gravity waves calculated from data of Paulino et al. (2018) taken from 2012-2014 in the Brazilian sector in the rising phase of the solar cycle 24.

Paulino's Table 1, the horizontal wavelength is 170.7 km and the intrinsic period is 20.7 min. From our simulation running with background parameters for the Paulino's observatory location for July 16, 2012, we have determined that $g = 9.06$ m/s, $H = 44.82$ km, $c_s = \gamma g H = 753.18$ m/s, $N = 0.00969171$ rad/s, and $f = -1.8784 \times 10^{-5}$ rad/s. Plugging these values into Eq. 2 and taking the square root, we obtain $m = 5.96 \times 10^{-5}$ rad/m, which corresponds to a vertical wavelength of 105.3 km.

By using the same background atmosphere conditions as for Fig. 9 and varying the intrinsic wave period in our model, we have found how the threshold vertical wavelength and the cancellation factor change with these two TID attributes (Fig. 10). For instance, the cancellation factor in the amplification regime ($\lambda_z > \lambda_z^t$) is much stronger (CF$\sim$1.8) in the short wave period range (10-20 min) than that in the longer wave period range ($\tau_i > 20$ min), where CF$\sim$1.1. We also notice that λ_z^t grows rapidly in the shorter wave period range (up to 70 min), then it tends to stabilize in a more steady value ($\lambda_z^t \sim 375$ km) for periods longer than 70 min.

Fig. 10 permits a direct comparison with Fig. 9 from where we have obtained good agreement with the observational data. The distribution in Fig. 9 shows maximal occurrence of TID wavelengths within the range of 144-168 km. If we analyse the period distribution of the Paulino's events, we verify that most of them (16 out of 24 events) fall in the range of 10-20 min (14.7 min in average). Observe in Fig. 10 that for $\tau_i \sim 14.7$

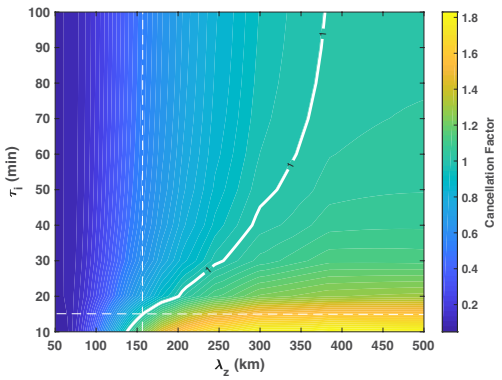

Figure 10. Variation of the cancellation factor with the vertical wavelength and the intrinsic period of TID. The diagram was composed by taking the same atmospheric conditions utilized in Fig. 9. The thick continuous line represents where CF=1. The vertical dashed line represents the threshold vertical wavelength of ∼160 km for a wave period of ∼14.7 min (horizontal dashed line).

min, the threshold wavelength is ∼160 km. This is consistent with the maximal range distribution found for Paulino et al. (2018) events in Fig. 9.

Wavelengths smaller than 160 km would pose an observational challenge for ground-based measurements given the cancellation effect discussed earlier. However, Fig. 9 still shows a number of TID events having λ_z <96 km. It is possible that TID would still be detectable even under the attenuation regime ($\lambda_z < \lambda_z^t = 160$ km) if they present sufficiently large amplitudes, which can occur when waves are near critical levels where the wave action is absorbed (Gossard & Hooke, 1975). In fact, Paulino et al. (2018) show a number of TID events with intrinsic period close to the Brunt-Väisälä period τ_N, indicating those events were close to critical levels. Near these critical levels, the vertical wavelength of waves shrinks, which would explain the presence of smaller vertical scale waves in the distribution. Also, as waves approach critical levels, the amplitude increases to compensate for the shrinking effect in λ_z (Gossard & Hooke, 1975). Supposedly, the signal from the airglow would then be enhanced, making these waves observable.

Another possible explanation for the shorter vertical wavelengths is that large scale waves like atmospheric tides would act on the O(^1D) emission causing variations in the layer's thickness in a manner similar to that demonstrated in Fig. 4b. As the layer thins

down within the wave cycle, it would be possible to observe shorter vertical scale waves at the instant the layer gets sufficiently thinner.

It is also possible that the vertical small scale TID events in Fig. 9 have been mistaken for gravity waves in the mesosphere. This could be the case when the O(^1D) thermospheric signal is contaminated by the mesospheric OH(9-3) band signal recorded by all-sky imagers. This possibly occurs as the mesospheric OH(9-3) has a marked brightness peak at 630 nm and a mean intensity 25% that of the thermospheric redline. In fact, this contamination has been noticed in our nightglow measurements at the Andes Lidar Observatory, were we run all-sky imagers equipped with filters for the OH and the redline running sequentially. In nights of large wave activity in the OH emission, we have observed the presence of the exact same wave structures in redline images—a clear indication that the contamination occurs. Thus, a cross-check between sequential OH and redline images would be necessary to confirm that the observed TID are in fact propagating across the thermosphere at a given instant.

5 Conclusion

This paper has reported our simulations of the thermospheric redline nightglow emission under the influence of oscillations of various vertical scales and under distinctive solar activity conditions. The goal here was to understand which waves perturbing the redline emission would be more likely to be detected in ground-based nightglow measurements. We have also compared the results with observations of TID activity in the thermosphere registered in the redline imagery. The main findings of this work are as follows:

- Under general background conditions and solar activity, we have found that TID, or gravity waves, perturbing the redline emission will be more likely seen if they present relatively large vertical wavelengths. Waves having λ_z >160 km will be promptly detectable.
- Also under general conditions, waves of smaller vertical scales (λ_z <160 km) would be observed only if they present larger amplitudes, that is, amplitude large enough to compensate for the attenuation (or cancellation effect) caused by the redline layer structure on the wave amplitude (in intensity) when measured from the ground.

- Waves presenting long vertical scales ($\lambda_z > \lambda_z^t$) would be more likely detectable from the ground because the layer response in radiance is amplified due to the photochemistry of the redline emission. This amplification effect is much smaller than those calculated for the mesospheric nightglow layers (Vargas et al., 2007).
- As the solar activity intensifies, the scales of the most likely observable waves in the redline shift to ever larger vertical wavelengths. Under high solar activity conditions, only waves presenting vertical wavelengths larger than 360 km would be likely observed because the redline layer structure gets thicker and the layer peak shifts to higher altitudes, reinforcing the estimated cancellation effect.
- The increase of the molecular oxygen density in the thermosphere during high solar activity periods is the dominant factor to account for the increased thickness and peak altitude of the O(^1D) layer.
- We have found a favorable correspondence between the most likely observable TID vertical wavelengths from the simulation and those of the observation (Negale et al., 2018; Paulino et al., 2018). The distribution of observed wavelengths peaks in the vertical wavelength range approximately equal to or larger than the range of the predicted threshold wavelength λ_z^t =160 km.
- The low occurrence rate of MSTID in measurements of the O(^1D) during high solar cycle can be explained by the stronger layer cancellation effect during high solar cycle—an effect caused by changes in the redline layer structure in combination with a smaller occurrence of long vertical wavelength waves (Negale et al., 2018).

Acknowledgments

This research has been supported by the National Science Foundation under 1- NSF AGS Grant 17-59573 and 2- NSF AGS Grant 19-03336. Data of the NRLMSISE-00 Atmospheric Model were obtained from https://ccmc.gsfc.nasa.gov/modelweb/models/nrlmsise00.php. Data of the International Reference Ionosphere - IRI2016 were obtained from https://ccmc.gsfc.nasa.gov/modelweb/models/iri2016_vitmo.php. We would like to express our deep appreciation to two anonymous reviewers by providing important insights to improve the present work.

References

Berrington, K., & Burke, P. (1981). Effective collision strengths for forbidden transitions in e-N and e-O scattering. *Planetary and Space Science*, *29*(3), 377 - 381.

Bowman, G. G. (1992). Upper atmosphere neutral-particle density variations compared with spread-F occurrence rates at locations around the world. *Annales Geophysicae*.

Candido, C. M. N., Pimenta, A. A., Bittencourt, J. A., & Becker-Guedes, F. (2008). Statistical analysis of the occurrence of medium-scale traveling ionospheric disturbances over brazilian low latitudes using oi 630.0 nm emission all-sky images. *Geophysical Research Letters*, *35*(17). doi: 10.1029/2008GL035043

Chen, A., Johnsen, R., & Biondi, M. A. (1978). Measurements of the O^++ N2 and O^++ O2 reaction rates from 300 to 900 k. *The Journal of Chemical Physics*, *69*(6), 2688-2691. doi: 10.1063/1.436917

Duly, T. M., Chapagain, N. P., & Makela, J. J. (2013). Climatology of nighttime medium-scale traveling ionospheric disturbances (mstids) in the central pacific and south american sectors. *Annales Geophysicae*, *31*(12), 2229–2237. doi: 10.5194/angeo-31-2229-2013

Fedorenko, Y. P., Tyrnov, O. F., Fedorenko, V. N., & Dorohov, V. L. (2013). Model of traveling ionospheric disturbances. *J. Space Weather Space Clim.*, *3*, A30. doi: 10.1051/swsc/2013052

Ferguson, E. E. (1974). Laboratory measurements of ionospheric ion-molecule reaction rates. *Reviews of Geophysics*, *12*(4), 703-713. doi: 10.1029/RG012i004p00703

Francis, S. H. (1974). A theory of medium-scale traveling ionospheric disturbances. *Journal of Geophysical Research (1896-1977)*, *79*(34), 5245-5260. doi: 10.1029/JA079i034p05245

Garcia, F. J., Kelley, M. C., Makela, J. J., & Huang, C.-S. (2000). Airglow observations of mesoscale low-velocity traveling ionospheric disturbances at midlatitudes. *Journal of Geophysical Research: Space Physics*, *105*(A8), 18407-18415. doi: 10.1029/1999JA000305

Gossard, E., & Hooke, W. (1975). *Waves in the atmosphere: atmospheric infrasound and*

gravity waves : their generation and propagation. Elsevier Scientific Pub. Co. Retrieved from https://books.google.com/books?id=pydRAAAAMAAJ

Hines, C. O. (1960). Internal atmospheric gravity waves at ionospheric heights. *Canadian Journal of Physics*, *38*(11), 1441-1481. doi: 10.1139/p60-150

Hooke, W. (1968). Ionospheric irregularities produced by internal atmospheric gravity waves. *Journal of Atmospheric and Terrestrial Physics*, *30*(5), 795 - 823.

Hooke, W. H. (1970). The ionospheric response to internal gravity waves: 1. the F2 region response. *Journal of Geophysical Research*, *75*(28), 5535–5544.

Klausner, V., Fagundes, P. R., Sahai, Y., Wrasse, C. M., Pillat, V. G., & Becker-Guedes, F. (2009). Observations of GW/TID oscillations in the F2 layer at low latitude during high and low solar activity, geomagnetic quiet and disturbed periods. *Journal of Geophysical Research: Space Physics*, *114*(A2). doi: 10.1029/2008JA013448

Kotake, N., Otsuka, Y., Ogawa, T., Tsugawa, T., & Saito, A. (2007, Feb 01). Statistical study of medium-scale traveling ionospheric disturbances observed with the gps networks in southern california. *Earth, Planets and Space*, *59*(2), 95–102. doi: 10.1186/BF03352681

Kubota, M., Conde, M., Ishii, M., Murayama, Y., & Jin, H. (2011). Characteristics of nighttime medium-scale traveling ionospheric disturbances observed over alaska. *Journal of Geophysical Research: Space Physics*, *116*(A5). doi: 10.1029/2010JA016212

Lakshmi Narayanan, V., Shiokawa, K., Otsuka, Y., & Saito, S. (2014). Airglow observations of nighttime medium-scale traveling ionospheric disturbances from yonaguni: Statistical characteristics and low-latitude limit. *Journal of Geophysical Research: Space Physics*, *119*(11), 9268-9282. doi: 10.1002/2014JA020368

Link, R., & Cogger, L. L. (1988). A reexamination of the O I 6300-Å nightglow. *Journal of Geophysical Research: Space Physics*, *93*(A9), 9883-9892. doi: 10.1029/JA093iA09p09883

Martinis, C., Baumgardner, J., Wroten, J., & Mendillo, M. (2010, 6). Seasonal dependence of MSTIDs obtained from 630.0 nm airglow imaging at arecibo. *Geophysical Research Letters*, *37*(11). doi: 10.1029/2010GL043569

Martyn, D. F. (1950). The morphology of the ionospheric variations associated with

magnetic disturbance. i. variations at moderately low latitudes. *Proceedings of the Royal Society of London Series A*, *218*, 1-18. doi: 10.1098/rspa.1953.0082

Munro, G. (1950). Travelling disturbances in the ionosphere. *Proceedings of the Royal Society of London Series A*, *202*, 208-223. doi: 10.1098/rspa.1950.0095

Munro, G. H. (1958). Travelling ionospheric disturbances in the F region. *Australian Journal of Physics*, *11*, 91-112. doi: 10.1071/PH580091

Negale, M. R., Taylor, M. J., Nicolls, M. J., Vadas, S. L., Nielsen, K., & Heinselman, C. J. (2018). Seasonal propagation characteristics of MSTIDs observed at high latitudes over central alaska using the poker flat incoherent scatter radar. *Journal of Geophysical Research: Space Physics*, *123*(7), 5717-5737. doi: 10.1029/2017JA024876

Nishioka, M., Saito, A., & Tsugawa, T. (2009). Super-medium-scale traveling ionospheric disturbance observed at midlatitude during the geomagnetic storm on 10 November 2004. *Journal of Geophysical Research: Space Physics*, *114*(A7). doi: 10.1029/2008JA013581

Ogawa, T., Balan, N., Otsuka, Y., Shiokawa, K., Ihara, C., Shimomai, T., & Saito, A. (2002). Observations and modeling of 630 nm airglow and total electron content associated with traveling ionospheric disturbances over Shigaraki, Japan. *Earth Planets Space*, *54*, 45-56.

Park, J., Lühr, H., Min, K. W., & Lee, J.-J. (2010). Plasma density undulations in the nighttime mid-latitude f-region as observed by CHAMP, KOMPSAT-1, and DMSP F15. *Journal of Atmospheric and Solar-Terrestrial Physics*, *72*(2), 183 - 192. doi: https://doi.org/10.1016/j.jastp.2009.11.007

Paulino, I., Medeiros, A. F., Vadas, S. L., Wrasse, C. M., Takahashi, H., Buriti, R. A., ... Gobbi, D. (2016). Periodic waves in the lower thermosphere observed by OI630 nm airglow images. *Annales Geophysicae*, *34*(2), 293–301. doi: 10.5194/angeo-34-293-2016

Paulino, I., Moraes, J. F., Maranhão, G. L., Wrasse, C. M., Buriti, R. A., Medeiros, A. F., ... Campos, J. A. V. (2018). Intrinsic parameters of periodic waves observed in the OI6300 airglow layer over the Brazilian equatorial region. *Annales Geophysicae*, *36*(1), 265–273. doi: 10.5194/angeo-36-265-2018

Perkins, F. (1973). Spread f and ionospheric currents. *Journal of Geophysical Research (1896-1977)*, *78*(1), 218-226. doi: 10.1029/JA078i001p00218

Pimenta, A. A., Amorim, D. C. M., & Candido, C. M. N. (2008). Thermospheric dark band structures at low latitudes in the southern hemisphere under different solar activity conditions: A study using OI 630 nm emission all-sky images. *Geophysical Research Letters*, *35*(16). doi: 10.1029/2008GL034904

Porter, H. S., Silverman, S. M., & Tuan, T. F. (1974). On the behavior of airglow under the influence of gravity waves. *Journal of Geophysical Research (1896-1977)*, *79*(25), 3827-3833. doi: 10.1029/JA079i025p03827

Shiokawa, K., Ihara, C., Otsuka, Y., & Ogawa, T. (2003). Statistical study of nighttime medium-scale traveling ionospheric disturbances using midlatitude airglow images. *Journal of Geophysical Research: Space Physics*, *108*(A1). doi: 10.1029/2002JA009491

Shiokawa, K., Otsuka, Y., & Ogawa, T. (2006). Quasiperiodic southward moving waves in 630-nm airglow images in the equatorial thermosphere. *Journal of Geophysical Research: Space Physics*, *111*(A6). doi: 10.1029/2005JA011406

Shiokawa, K., Otsuka, Y., & Ogawa, T. (2009). Propagation characteristics of nighttime mesospheric and thermospheric waves observed by optical mesosphere thermosphere imagers at middle and low latitudes. *Earth, Planets and Space*, *61*(4), 479–491.

Sobral, J., Takahashi, H., Abdu, M., Muralikrishna, P., Sahai, Y., & Zamlutti, C. (1992). O(1S) and O(1D) quantum yields from rocket measurements of electron densities and 557.7 and 630.0 nm emissions in the nocturnal f-region. *Planetary and Space Science*, *40*(5), 607 - 619.

Streit, G. E., Howard, C. J., Schmeltekopf, A. L., Davidson, J. A., & Schiff, H. I. (1976). Temperature dependence of O(1D) rate constants for reactions with O2, N2, CO2, O3, and H2O. *The Journal of Chemical Physics*, *65*(11), 4761-4764. doi: 10.1063/1.432930

Swenson, G., Yee, Y., Vargas, F., & Liu, A. (2018). Vertical diffusion transport of atomic oxygen in the mesopause region consistent with chemical losses and continuity: Global mean and inter-annual variability. *Journal of Atmospheric and Solar-Terrestrial Physics*, *178*, 47 - 57. doi: 10.1016/j.jastp.2018.05.014

Takeo, D., Shiokawa, K., Fujinami, H., Otsuka, Y., Matsuda, T. S., Ejiri, M. K., ... Yamamoto, M. (2017). Sixteen year variation of horizontal phase velocity and propagation direction of mesospheric and thermospheric waves in airglow images at Shigaraki, Japan. *Journal of Geophysical Research: Space Physics*, *122*(8), 8770-8780. doi: 10.1002/2017JA023919

Taylor, M. J., Jahn, J.-M., Fukao, S., & Saito, A. (1998). Possible evidence of gravity wave coupling into the mid-latitude F region ionosphere during the SEEK campaign. *Geophysical Research Letters*, *25*(11), 1801-1804. doi: 10.1029/97GL03448

Torr, D. G., Torr, M. R., Walker, J. C. G., Brace, L. H., Brinton, H. C., Hanson, W. B., ... Oppenheimer, M. (1976). Recombination of NO+ in the ionosphere. *Geophysical Research Letters*, *3*(4), 209-212. doi: 10.1029/GL003i004p00209

Torr, D. G., Torr, M. R., Walker, J. C. G., Nier, A. O., Brace, L. H., & Brinton, H. C. (1976). Recombination of O2+ in the ionosphere. *Journal of Geophysical Research (1896-1977)*, *81*(31), 5578-5580. doi: 10.1029/JA081i031p05578

Vargas, F., Swenson, G., Liu, A., & Gobbi, D. (2007). O(1S), OH, and O2(b) airglow layer perturbations due to AGWs and their implied effects on the atmosphere. *Journal of Geophysical Research: Atmospheres*, *112*(D14). doi: 10.1029/2006JD007642

Vickers, H., Kosch, M. J., Sutton, E., Bjoland, L., Ogawa, Y., & La Hoz, C. (2014). A solar cycle of upper thermosphere density observations from the EISCAT svalbard radar. *Journal of Geophysical Research: Space Physics*, *119*(8), 6833-6845. doi: 10.1002/2014JA019885

Yee, J., Guberman, S. L., & Dalgarno, A. (1990). Collisional quenching of O(1D) by O(3P). *Planetary and Space Science*, *38*(5), 647 - 652.

Yokoyama, T., & Hysell, D. L. (2010). A new midlatitude ionosphere electrodynamics coupling model (MIECO): Latitudinal dependence and propagation of medium-scale traveling ionospheric disturbances. *Geophysical Research Letters*, *37*(8). doi: 10.1029/2010GL042598